

Communication

2-D Electromagnetic Scattering and Inverse Scattering from Magnetodielectric Objects Based on Integral Equation Method

Tian Lan^{ID}, Na Liu^{ID}, Yanhui Liu^{ID}, Feng Han^{ID}, and Qing Huo Liu^{ID}

Abstract—Efficient 2-D full-waveform forward and inverse electromagnetic scattering solvers are presented in this communication. The combined field volume integral equation (CFVIE) is formulated in a layered medium. Different from the previous work, the mixed-order basis function is adopted in the discretization of the 2-D CFVIE. Meanwhile, the permittivity and permeability are simultaneously reconstructed in the inversion through the variational Born iteration method, which is enhanced with a self-adaptive regularization factor and applied to the multifrequency data. The proposed forward solver is validated by comparisons with the finite-element simulations.

Index Terms—2-D combined field volume integral equation (CFVIE), inverse scattering, magnetodielectric materials, variational Born iteration method (VBIM).

I. INTRODUCTION

Electromagnetic (EM) scattering and inverse scattering have been intensively studied in recent years due to their wide applications in geophysical prospecting, medical diagnosis, nondestructive evaluation, and so on. In the forward scattering, it is assumed that dielectric parameters of the scatterers are known and the EM fields are to be solved, while the process of inversion is to reconstruct the EM parameters in the domain of interest without access to the interior.

One of the most popular methods to solve the EM scattering problem is the method of moment (MoM) based on the volume integral equation (VIE). MoM has no absorbing boundary condition and does not include the transmitters and receivers in the computation domain, which decreases the unknowns in the solving process. However, direct matrix inversion in the MoM usually has a high computation cost [1]. Iterative methods such as biconjugate gradient (CG) stabilized (BCGS) [2] are preferred. The inverse scattering problems are generally nonlinear and ill-posed. Various methods have been proposed to solve EM inverse problems, such as the Born iteration method (BIM) [3], contrast source inversion [4], subspace-based optimization method [5], and so on. The variational BIM (VBIM) is based on VIE, which is first proposed in [6] and shows the merit of stability and high efficiency, particularly for low-scattering objects. These inversion methods are mainly applied in dielectric inversion. In recent years, the interest to image magnetodielectric objects is increasing in many engineering applications, including biomedical imaging [7], [8], geophysical exploration [9], [10], and so on.

Manuscript received January 18, 2018; revised October 15, 2018; accepted November 10, 2018. Date of publication November 27, 2018; date of current version February 5, 2019. This work was supported by the National Natural Science Foundation of China under Grant 41390453, Grant 11501481, and Grant 41504120. (*Corresponding authors:* Feng Han; Qing Huo Liu.)

T. Lan, N. Liu, and F. Han are with the Institute of Electromagnetics and Acoustics, Department of Electronic Science, Xiamen University, Xiamen 361005, China (e-mail: feng.han@xmu.edu.cn).

Y. Liu is with the Institute of Electromagnetics and Acoustics, Department of Electronic Science, Xiamen University, Xiamen 361005, China, and also with the Global Big Data Technologies Centre, University of Technology Sydney, Ultimo, NSW 2007, Australia.

Q. H. Liu is with the Department of Electrical and Computer Engineering, Duke University, Durham, NC 27708 USA (e-mail: qqliu@duke.edu).

Color versions of one or more of the figures in this communication are available online at <http://ieeexplore.ieee.org>.

Digital Object Identifier 10.1109/TAP.2018.2883586

Previously, the VIE method through BCGS fast Fourier transform (FFT) is used to solve the 3-D EM magnetodielectric scattering problems [11]. Meanwhile, the inverse scattering of magnetodielectric objects embedded in a homogeneous background at a single frequency is also studied in [12]. Compared with the single-frequency inversion, the multifrequency inversion is more stable. There are two strategies in multifrequency inversion, the frequency-hopping and simultaneous inversion. The frequency-hopping strategy uses the inversion results from the low frequency as the initial model of the high-frequency inversion [13]. Therefore, it finds the best fit about the measurement data in the highest frequency in the final results and shows some misfits in the low-frequency range, especially when there are more inversion parameters, such as in magnetodielectric inversion. Whereas the simultaneous multifrequency inversion tries to match all the data in different sampling frequencies and gives the multiscale image results, it has been adopted in inverse problems in recent years [14].

In most of these previous research works, both the forward BCGS-FFT simulation and inverse scattering about magnetodielectric objects are performed in a 3-D domain in a homogeneous background. In this communication, we study the 2-D EM scattering and reconstruct both permittivity and permeability of objects embedded in the background medium, which can be either homogeneous or layered. Compared with the EM scattering solver in a homogeneous background, the 2-D solver in a layered medium can be applied in the through-wall imaging [15], cross-well reservoir monitoring [16], and so on. In the forward scattering problem, the 2-D combined field VIE (CFVIE) is formulated, and the 2-D mixed-order basis function is adopted to expand the flux densities and the vector potentials. The scattered fields computed from the CFVIE are compared to the commercial software COMSOL simulations based on the finite-element method. In the next step, we use the simultaneous multifrequency inversion with a self-adaptive regularization factor to achieve the reconstruction of 2-D multiscale objects in air and through-wall backgrounds.

II. METHODS

A. Forward Method

The Helmholtz equations for the magnetic vector potential \mathbf{A} and the electric vector potential \mathbf{F} in the background medium are express as [17]

$$\nabla^2 \mathbf{A} + k_b^2 \mathbf{A} = -\mu_b \mathbf{J} \quad (1a)$$

$$\nabla^2 \mathbf{F} + k_b^2 \mathbf{F} = -\epsilon_b \mathbf{M} \quad (1b)$$

whose solutions are $\mathbf{A} = \mathbf{G}^{AJ} \otimes \mathbf{J}$ and $\mathbf{F} = \mathbf{G}^{FM} \otimes \mathbf{M}$. k_b is the wavenumber in the background medium. In this communication, we only focus on 2-D TMz wave illumination. The variables \mathbf{A} , \mathbf{E} , and \mathbf{D} only have \hat{z} components, while the variables \mathbf{F} , \mathbf{H} , and \mathbf{B} have both \hat{x} and \hat{y} components. \mathbf{G}^{AJ} and \mathbf{G}^{FM} are 2-D dyadic Green's functions for vector potentials \mathbf{A} and \mathbf{F} , respectively. The 3-D layered dyadic Green functions are given in [18]. In the 2-D case, they can

be derived in a similar way. The main difference is the transform from the spectral domain to the spatial domain. The transforms are expressed as

$$f_e(x; y) = \frac{j\omega}{\pi} \int_0^{+\infty} \tilde{f}_e(k_x; y) \cos(k_x x) dk_x \quad (2a)$$

$$f_o(x; y) = -\frac{\omega}{\pi} \int_0^{+\infty} \tilde{f}_o(k_x; y) \sin(k_x x) dk_x \quad (2b)$$

where \tilde{f} is the spectral form, while f represents the spatial form. The subscripts e and o denote the even and odd modes, respectively. Due to the odd or even symmetry of different components in Green's functions, the transforms about $\tilde{G}^{H_y J_z}, \tilde{G}^{H_y M_x}, \tilde{G}^{E_z M_y}$, and $\tilde{G}^{H_x M_y}$ follow the odd transform (2b), and the others follow the even transform (2a). The detailed expressions of Green's function in the spectral domain are the same as those given in [18].

Once Green's functions are computed, the scattered vector potentials due to contrasts with respect to the background can be obtained through their convolution with the equivalent current sources $\mathbf{J} = j\omega\chi^\epsilon \mathbf{D}$ and $\mathbf{M} = j\omega\chi^\mu \mathbf{B}$

$$\mathbf{A} = \frac{1}{\epsilon_b} \int_{\Omega} \chi^\epsilon(\mathbf{r}') \mathbf{D}(\mathbf{r}') \mathbf{G}^{AJ}(\mathbf{r}, \mathbf{r}') d\mathbf{r}' \quad (3a)$$

$$\mathbf{F} = \frac{1}{\mu_b} \int_{\Omega} \chi^\mu(\mathbf{r}') \mathbf{B}(\mathbf{r}') \mathbf{G}^{FM}(\mathbf{r}, \mathbf{r}') d\mathbf{r}' \quad (3b)$$

where $\chi^\epsilon = (\epsilon - \epsilon_b)/\epsilon$ is the electric contrast and $\chi^\mu = (\mu - \mu_b)/\mu$ is the magnetic contrast. The CFVIEs are formulated as

$$\mathbf{E}^{inc} = \mathbf{D}/\epsilon - (k_b^2 + \nabla \nabla \cdot) \mathbf{A} + j\omega\mu_b \nabla \times \mathbf{F} \quad (4a)$$

$$\mathbf{H}^{inc} = \mathbf{B}/\mu - big(k_b^2 + \nabla \nabla \cdot) \mathbf{F} - j\omega\epsilon_b \nabla \times \mathbf{A}. \quad (4b)$$

In order to solve the CFVIE in (4), we need to discretize the computation domain and acquire the weak forms of (4). To conveniently express the basis function and test function, we denote the axes x , y , and z as x_1 , x_2 , and x_3 in the remaining discussion. We divide the bounded domain $L_1 \times L_2$ into $N_1 \times N_2$ rectangle cells of the area $\Delta s = \Delta x_1 \Delta x_2$.

Considering the divergence-conforming property of \mathbf{D} and \mathbf{B} , and the curl operation on \mathbf{A} and \mathbf{F} , we need two groups of basis functions including divergence-conforming Ψ and curl-conforming Φ to expand \mathbf{D} , \mathbf{B} , \mathbf{A} , and \mathbf{F} . The divergence-conforming basis functions are given as follows:

$$\begin{aligned} \psi_{k,l}^{(1)} &= \Lambda(x_1 - k\Delta x_1; 2\Delta x_1) \\ &\times \Pi(x_2 - (l - 0.5)\Delta x_2; \Delta x_2) \end{aligned} \quad (5a)$$

$$\begin{aligned} \psi_{k,l}^{(2)} &= \Pi(x_1 - (k - 0.5)\Delta x_1; \Delta x_1) \\ &\times \Lambda(x_2 - l\Delta x_2; 2\Delta x_2) \end{aligned} \quad (5b)$$

$$\begin{aligned} \psi_{k,l}^{(3)} &= \Pi(x_1 - (k - 0.5)\Delta x_1; \Delta x_1) \\ &\times \Pi(x_2 - (l - 0.5)\Delta x_2; \Delta x_2) \end{aligned} \quad (5c)$$

where $\Pi(x; \Delta x)$ is a pulse function centered at x with the support Δx , and $\Lambda(x; 2\Delta x)$ is a triangle function centered at x with the support $2\Delta x$. Then, \mathbf{D} and \mathbf{B} are expressed as

$$D_3(\mathbf{r}) = \epsilon_b \sum_{k,l} d_{k,l}^{(3)} \psi_{k,l}^{(3)}(\mathbf{r}) \quad (6a)$$

$$B_{1,2}(\mathbf{r}) = \mu_b \sum_{k,l} b_{k,l}^{(1,2)} \psi_{k,l}^{(1,2)}(\mathbf{r}). \quad (6b)$$

Then, for the curl-conforming basis function $\phi_{k,l}$ defined in cell (k, l) , we adopt the mixed-order Lagrange-type function as

$$\phi_{k,l,i,j}^{(1)} = \phi_{k,i}^{(1)}(x_1) \phi_{l,j}^{(2)}(x_2) \quad (7a)$$

$$\phi_{k,l,i,j}^{(2)} = \phi_{k,i}^{(2)}(x_1) \phi_{l,j}^{(1)}(x_2) \quad (7b)$$

$$\phi_{k,l,i,j}^{(3)} = \phi_{k,i}^{(2)}(x_1) \phi_{l,j}^{(2)}(x_2) \quad (7c)$$

where

$$\phi_{p,1}^{(1)}(x) = (1 - x')/2, \quad \phi_{p,2}^{(1)}(x) = (1 + x')/2 \quad (8a)$$

$$\phi_{p,1}^{(2)}(x) = x'(x' - 1)/2, \quad \phi_{p,2}^{(2)}(x) = 1 - x'^2 \quad (8b)$$

$$\phi_{p,3}^{(2)}(x) = x'(x' + 1)/2, \quad p = k, l \quad (8c)$$

and x' is defined in the range $[-1, 1]$ mapped from the original range $[(p - 1)\Delta x, p\Delta x]$. From (7), we can see that in the cell (k, l) , there are totally 2×3 basis functions in the direction \hat{x}_1 and \hat{x}_2 , and 3×3 basis functions in the direction \hat{x}_3 . The vector potentials \mathbf{A} and \mathbf{F} are expanded as

$$A_3(\mathbf{r}) = \sum_{k,l,i,j} a_{k,l,i,j}^{(3)} \phi_{k,l,i,j}^{(3)}(\mathbf{r}) \quad (9a)$$

$$F_{1,2}(\mathbf{r}) = \sum_{k,l,i,j} f_{k,l,i,j}^{(1,2)} \phi_{k,l,i,j}^{(1,2)}(\mathbf{r}). \quad (9b)$$

We then test both sides of (4) with the divergence-conforming basis function $\psi_{m,n}^{(\xi)}$ given in (5). Due to $\partial \psi / \partial x_3 = 0$, the term $\nabla \nabla \cdot \mathbf{A}$ is omitted. Then, we use Gauss's theorem to move one divergence operator from \mathbf{F} to $\psi_{m,n}$, and obtain

$$\begin{aligned} &\int_{\Omega} \psi_{m,n}^{(\xi)}(\mathbf{r}) \mathbf{E}^{inc}(\mathbf{r}) d\mathbf{r} \\ &= \int_{\Omega} \psi_{m,n}^{(\xi)}(\mathbf{r}) \mathbf{D}(\mathbf{r}) / \epsilon(\mathbf{r}) d\mathbf{r} - k^2 \int_{\Omega} \psi_{m,n}^{(\xi)}(\mathbf{r}) \mathbf{A}(\mathbf{r}) d\mathbf{r} \\ &\quad + j\omega\mu_b \int_{\Omega} \psi_{m,n}^{(\xi)}(\mathbf{r}) \nabla \times \mathbf{F} d\mathbf{r} \end{aligned} \quad (10a)$$

$$\begin{aligned} &\int_{\Omega} \psi_{m,n}^{(\xi)}(\mathbf{r}) \mathbf{H}^{inc}(\mathbf{r}) d\mathbf{r} \\ &= \int_{\Omega} \psi_{m,n}^{(\xi)}(\mathbf{r}) \mathbf{B}(\mathbf{r}) / \mu(\mathbf{r}) d\mathbf{r} \\ &\quad - k^2 \int_{\Omega} \psi_{m,n}^{(\xi)}(\mathbf{r}) \mathbf{F}(\mathbf{r}) d\mathbf{r} + \int_{\Omega} \partial_\xi \psi_{m,n}^{(\xi)}(\mathbf{r}) \nabla \cdot \mathbf{F}(\mathbf{r}) d\mathbf{r} \\ &\quad - j\omega\epsilon_b \int_{\Omega} \psi_{m,n}^{(\xi)}(\mathbf{r}) \cdot \nabla \times \mathbf{A}(\mathbf{r}) d\mathbf{r}. \end{aligned} \quad (10b)$$

Substituting (6) and (9) in (10), we obtain the weak forms of the integral equation

$$\begin{aligned} E_{3,m,n}^{inc} &= \sum_{k,l} \left[d_{k,l}^{(3)} u_{m,n;k,l}^{(3)} + j\omega\mu_b \sum_{i=1}^3 \sum_{j=1}^3 a_{k,l;i,j}^{(3)} v_{m,n;k,l,i,j}^{(3)} \right. \\ &\quad \left. + \sum_{i=1}^3 \sum_{j=1}^2 f_{k,l,i,j}^{(2)} \tau_{m,n;k,l,i,j}^{(3;1;2)} \right. \\ &\quad \left. - \sum_{i=1}^2 \sum_{j=1}^3 f_{k,l,i,j}^{(1)} \tau_{m,n;k,l,i,j}^{(3;2;1)} \right] \end{aligned} \quad (11a)$$

$$\begin{aligned} H_{1;m,n}^{inc} &= \sum_{k,l} \left[b_{k,l}^{(1)} u_{m,n;k,l}^{(1)} + j\omega\epsilon_b \sum_{i=1}^2 \sum_{j=1}^3 f_{k,l,i,j}^{(1)} v_{m,n;k,l,i,j}^{(1)} \right. \\ &\quad \left. + \frac{1}{j\omega\mu_b} \left(\sum_{i=1}^2 \sum_{j=1}^3 f_{k,l,i,j}^{(1)} w_{m,n;k,l,i,j}^{(1;1)} \right. \right. \\ &\quad \left. \left. + \sum_{i=1}^3 \sum_{j=1}^2 f_{k,l,i,j}^{(2)} w_{m,n;k,l,i,j}^{(1;2)} \right) \right. \\ &\quad \left. - \sum_{i=1}^3 \sum_{j=1}^3 a_{k,l,i,j}^{(3)} \tau_{m,n;k,l,i,j}^{(1;2)} \right] \end{aligned} \quad (11b)$$

$$\begin{aligned}
H_{2;m,n}^{inc} = & \sum_{k,l} \left[b_{k,l}^{(2)} u_{k,l;m,n}^{(2)} + j\omega\epsilon_b \sum_{i=1}^3 \sum_{j=1}^2 f_{k,l,i,j}^{(2)} v_{m,n;k,l,i,j}^{(2)} \right. \\
& + \frac{1}{j\omega\mu_b} \left(\sum_{i=1}^2 \sum_{j=1}^3 f_{k,l,i,j}^{(1)} w_{m,n;k,l,i,j}^{(2;1)} \right. \\
& + \sum_{i=1}^3 \sum_{j=1}^2 f_{k,l,i,j}^{(2)} w_{m,n;k,l,i,j}^{(2;2)} \Big) \\
& \left. + \sum_{i=1}^3 \sum_{j=1}^3 a_{k,l,i,j}^{(3)} \tau_{m,n;k,l,i,j}^{(2;1)} \right] \quad (11c)
\end{aligned}$$

in which

$$u_{m,n;k,l}^{(3)} = \int_{\Omega} \psi_{m,n}^{(3)}(\mathbf{r}) \frac{\epsilon_b}{\epsilon(\mathbf{r})} \psi_{k,l}^{(3)}(\mathbf{r}) d\mathbf{r} \quad (12a)$$

$$u_{m,n;k,l}^{(p)} = \int_{\Omega} \psi_{m,n}^{(p)}(\mathbf{r}) \frac{\mu_b}{\mu(\mathbf{r})} \psi_{k,l}^{(p)}(\mathbf{r}) d\mathbf{r} \quad (12b)$$

$$v_{m,n;k,l,i,j}^{(o)} = \int_{\Omega} \psi_{m,n}^{(o)}(\mathbf{r}) \phi_{k,l,i,j}^{(o)}(\mathbf{r}) d\mathbf{r} \quad (12c)$$

$$\tau_{m,n;k,l,i,j}^{(3;p;q)} = \int_{\Omega} \psi_{m,n}^{(3)}(\mathbf{r}) \cdot \partial_p \phi_{k,l,i,j}^{(q)}(\mathbf{r}) d\mathbf{r} \quad (12d)$$

$$w_{m,n;k,l,i,j}^{(p;p)} = \int_{\Omega} \partial_p \psi_{m,n}^{(p)}(\mathbf{r}) \partial_p \phi_{k,l,i,j}^{(p)}(\mathbf{r}) d\mathbf{r} \quad (12e)$$

$$w_{m,n;k,l,i,j}^{(p;q)} = \int_{\Omega} \partial_p \psi_{m,n}^{(p)}(\mathbf{r}) \partial_q \phi_{k,l,i,j}^{(q)}(\mathbf{r}) d\mathbf{r} \quad (12f)$$

$$\tau_{m,n;k,l,i,j}^{(p;q)} = \int_{\Omega} \psi_{m,n}^{(p)}(\mathbf{r}) \partial_q \phi_{k,l,i,j}^{(3)}(\mathbf{r}) d\mathbf{r} \quad (12g)$$

$$o = 1, 2, 3, \quad p, q = 1, 2, \quad p \neq q.$$

The detailed discretized expressions about (11) and (12) are given in the Appendix.

In the discretized CFVIE (11), the coefficients $d_{k,l}$ and $b_{k,l}$ are unknowns and they are solved by BCGS iterations [19]. In each iteration, the continuous form of the convolution integral in (3) is converted to discrete convolution between the coefficients $d_{k,l}$ and $b_{k,l}$, in (6) and Green's functions to obtain $a_{k,l,i,j}$ and $f_{k,l,i,j}$ in (9) which can be accelerated by FFT [20].

B. Inversion Method

In the inversion, we redefine the contrast $\chi_{\epsilon} = (\epsilon - \epsilon_b)/\epsilon_b$ and $\chi_{\mu} = (\mu - \mu_b)/\mu_b$ to keep the linear relationship between χ and ϵ, μ . The scattered electric field is expressed as

$$\begin{aligned}
\mathbf{E}^{sct}(\mathbf{r}) = & \int_{\Omega} \mathbf{G}^{EJ}(\mathbf{r}, \mathbf{r}') \chi_{\epsilon}(\mathbf{r}') \mathbf{E}(\mathbf{r}') d\mathbf{r}' \\
& - \int_{\Omega} \mathbf{G}^{EM}(\mathbf{r}, \mathbf{r}') \chi_{\mu}(\mathbf{r}') \mathbf{H}(\mathbf{r}') d\mathbf{r}'. \quad (13)
\end{aligned}$$

We take the variations of the scattered field about χ_{ϵ} and χ_{μ} and obtain

$$\begin{aligned}
\delta\mathbf{E}^{sct}(\mathbf{r}) \simeq & \int_{\Omega} \mathbf{G}^{EJ}(\mathbf{r}, \mathbf{r}') \mathbf{E}^{q-1}(\mathbf{r}') \delta\chi_{\epsilon}(\mathbf{r}') d\mathbf{r}' \\
& - \int_{\Omega} \mathbf{G}^{EM}(\mathbf{r}, \mathbf{r}') \mathbf{H}^{q-1}(\mathbf{r}') \delta\chi_{\mu}(\mathbf{r}') d\mathbf{r}' \quad (14)
\end{aligned}$$

where $\delta\mathbf{E}^{sct}$ means the misfit between the computed scattered field and the measured scattered field, and \mathbf{E}^{q-1} and \mathbf{H}^{q-1} are the total fields computed by BCGS in the last iteration step. Then, we get

$$\delta\mathbf{E}_{q-1}^{sct} = \mathbf{L}_{q-1} \delta\chi \quad (15)$$

where \mathbf{L}_{q-1} is an $M \times N$ matrix containing Green's functions and the total fields computed in the $(q-1)$ th step. The total cell number is $N_c = N_1 * N_2$. There are N_r receivers and N_t transmitters. With N_f

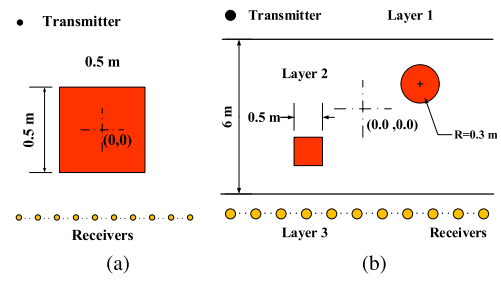


Fig. 1. Forward model in (a) homogeneous background media and (b) three-layered background media.

frequency points, the number of data points is $N_{tr} = N_r * N_t * N_f$. Therefore, we get $M = N_{tr}$ and $N = N_c * 2$ for the size of matrix \mathbf{L} . The cost function with the regularization term in the q th iteration step is defined as [21]

$$F(\delta\chi_q) = \|\delta\mathbf{E}_{q-1}^{sct} - \mathbf{L}_{q-1} \delta\chi_q\|^2 + \gamma^2 \frac{\|\delta\mathbf{E}_{q-1}^{sct}\|^2}{\|\delta\chi_{q-1}\|^2} \|\delta\chi_q\|^2. \quad (16)$$

Unlike in the previous VBIM [6], we introduce the self-adaptive regularization factor $\|\delta\mathbf{E}_{q-1}^{sct}\|^2 / \|\delta\chi_{q-1}\|^2$. On the one hand, the regularization factor decreases along with the decrease in scattered fields during the inversion process. On the other hand, the regularization factor increases when the change of contrast decrease. By this means, the process of inversion becomes more stable. This linear least-square problem of (16) is equivalent to [21]

$$\left(\mathbf{L}_{q-1}^{\dagger} \mathbf{L}_{q-1} + \frac{\gamma^2 \|\delta\mathbf{E}_{q-1}^{sct}\|^2}{\|\delta\chi_{q-1}\|^2} \mathbf{I} \right) \delta\chi_q = \mathbf{L}_{q-1}^{\dagger} \delta\mathbf{E}_{q-1}^{sct} \quad (17)$$

which can be solved by the CG method, where \dagger denotes the complex conjugate and transpose.

III. NUMERICAL RESULTS

In this section, we will validate the forward and inversion methods presented in Section II through the computation of EM scattering and inverse scattering in homogeneous and layered background media, respectively.

A. Forward Validation

In the first model, we simulate the EM scattering in the background of air. As shown in Fig. 1(a), there is a square scatterer with the center in $(0.0, 0.0)$, and the side length of 0.5 m. The relative permittivity and permeability of the scatterer are $\epsilon_r = 2.0$ and $\mu_r = 2.0$, respectively. The transmitter is located at $(-1.0, 1.0)$ m. There are 41 receivers distributed uniformly from $(-1.0, -1.0)$ m to $(1.0, -1.0)$ m. To verify our 2-D forward BCGS-FFT solver, we choose the frequency of 150 MHz. The computation domain is a 1 m \times 1 m square wrapping the scatterer. There are 40×40 cells in the domain. The scattered fields in the 41 receivers from CFVIE and COMSOL simulations are shown in Fig. 2. Clearly, the results match well. To quantitatively evaluate the accuracy of the forward solver, we define the relative error of scattered field as

$$\text{Err} = \frac{\|f_{\text{CFVIE}}^{\text{sct}} - f_{\text{COMSOL}}^{\text{sct}}\|}{\|f_{\text{COMSOL}}^{\text{sct}}\|} \quad (18)$$

where $\|\cdot\|$ means the $L-2$ norm, and f can be one component of the electric field \mathbf{E} or the magnetic field \mathbf{H} . In this model, the relative errors are 0.34% for E_3^{sct} , 0.32% for H_1^{sct} , and 0.37% for H_2^{sct} .

For the second model, we will verify our 2-D forward solver in a three-layered background medium. As shown in Fig. 1(b), there are two

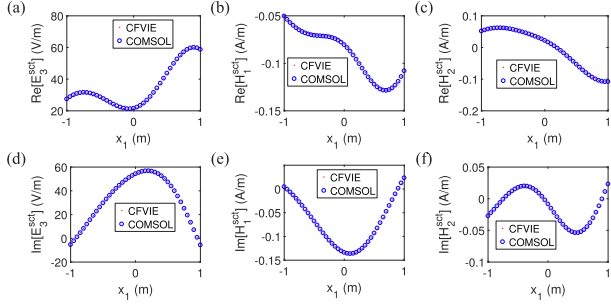


Fig. 2. Comparisons between CFVIE and COMSOL simulations of the scattered fields in homogeneous background media. Real part of (a) E_3^{sct} , (b) H_1^{sct} , and (c) H_2^{sct} . Image part of (d) E_3^{sct} , (e) H_1^{sct} , and (f) H_2^{sct} .

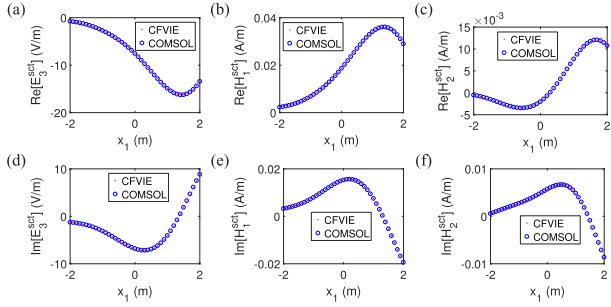


Fig. 3. Comparisons between CFIE and COMSOL simulations of the scattered fields in three-layered background. Real part of (a) E_3^{sct} , (b) H_1^{sct} , and (c) H_2^{sct} . Image part of (d) E_3^{sct} , (e) H_1^{sct} , and (f) H_2^{sct} .

scatterers in the middle layer. The left scatterer is a square with the side length of 0.5 m. The right scatterer is a disk of radius 0.3 m. The EM parameters of scatterers are $\epsilon_r = 2$ and $\mu_r = 2$, respectively. The pairs of relative permittivity and relative permeability from the top layer to the bottom layer are (1.3, 1.1), (1.0, 1.0), and (1.2, 1.5), respectively. The transmitter is located at $(-2.0, 4.0)$ m. 41 receivers are uniformly distributed from $(-2.0, -3.5)$ m to $(2.0, -3.5)$ m. The operating frequency of the transmitter is 100 MHz. The computation domain is a $3 \text{ m} \times 3 \text{ m}$ square wrapping two scatterers. There are 120×120 cells in the domain. The comparisons of the scattered fields at the receiver array between CFVIE and COMSOL simulations are shown in Fig. 3. Similar to the last model, they match well. The relative errors are 0.58% for E_3^{sct} , 0.59% for H_1^{sct} , and 0.61% for H_2^{sct} .

B. Inversion Assessment

In this section, we use two different models in homogeneous and layered background media to test our inversion algorithm. The regularization factor γ in (16) is set to be 0.1.

The first two inversion models are shown in Fig. 4, in which the scatterer is the classical Osterreich profile [15]. In the first model, the background is air. The scatterers have the EM parameters $\epsilon_r = 1.5$ and $\mu_r = 1.5$. We use 20 transmitters and 20 receivers surrounding the inverse domain in a circle, which is a typical configuration in magnetic resonance imaging. The operation frequencies are 100, 145, 190, and 235 MHz. We use the scattered field data acquired from our forward solver as the measured data. The inverted permittivity and permeability profiles are shown in Fig. 5(a) and (b), respectively. We can see the reconstructed objects fit well with the real profiles. The iteration number is 27. The misfit between the computed data and measured data is 0.95%. Then, we invert the profiles in the through-wall background. The parameters of the wall are $\epsilon_r = 2.0$ and $\mu_r = 1.2$. The parameters of the scatterers and the operating frequency keep the same as those in the last inversion model.

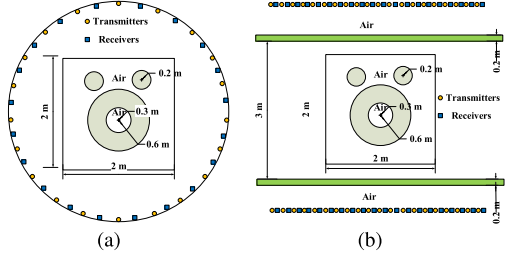


Fig. 4. Osterreich profile in (a) homogeneous and (b) through-wall-layered background.

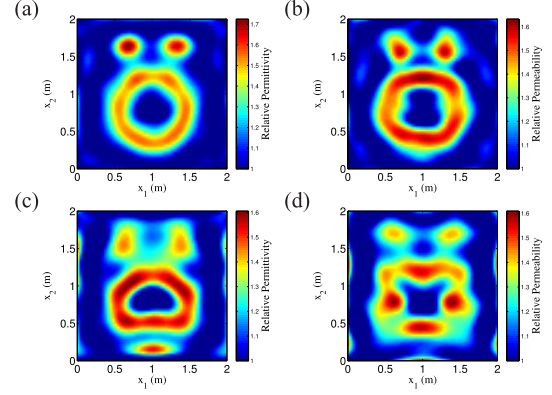


Fig. 5. Inversion results of Osterreich profile. The reconstructed profile of (a) permittivity and (b) permeability in homogeneous background. The reconstructed profile of (c) permittivity and (d) permeability in layered background.

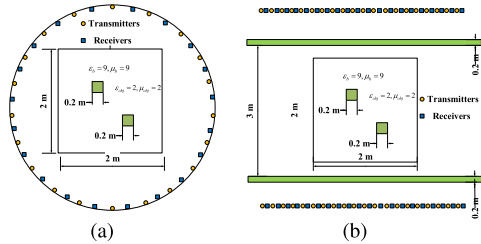


Fig. 6. Two cube profiles in (a) homogeneous and (b) through-wall-layered background.

There are 40 transmitters and 40 receivers located in the two sides of the wall. Compared with the circular receiver array in the last inversion model, the array aperture becomes smaller in this model. As shown in Fig. 5(c) and (d), the reconstructed profiles become worse than those in the last model. However, the basic shapes remain discernible. The inversion process terminates after 7 iterations when the residual error between the calculated scattered fields and the measured data is 4.9%.

In the following two models, we change the Osterreich profile into two small cubes with the parameters $\epsilon_r = 2.0$ and $\mu_r = 2.0$ which are located in the medium with $\epsilon_r = 9.0$ and $\mu_r = 9.0$. The operation frequencies are 10, 35, and 60 MHz. Therefore, it is a small but high-contrast scattering scenario. The configuration is shown in Fig. 6. Gauss white noise with SNR = 5 dB is added into the measured data for the inversion. The results are shown in Fig. 7. Because of the noise, the shapes of the scatterers become blurring, but their positions are correct. Due to the strong scattering, the sizes of inverted scatterers are bigger than those of the true scatterers, and the permittivity and permeability become larger. At this time, the residual error between the calculated scattered fields and the measured data

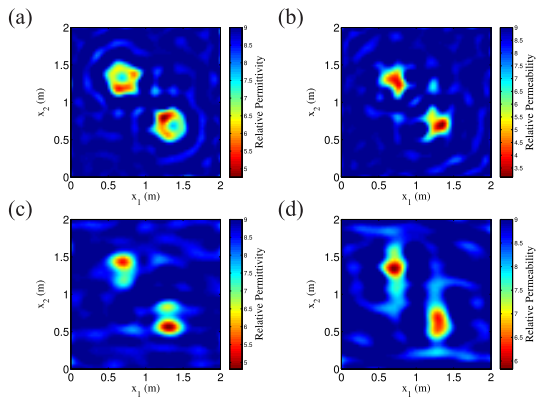


Fig. 7. Inversion results of two cube profiles. The reconstructed profile of (a) permittivity and (b) permeability in the homogeneous background. The reconstructed profile of (c) permittivity and (d) permeability in the layered background.

is 2.44% in the homogeneous background and 8.79% in the layered background.

IV. CONCLUSION

First, we achieve the 2-D CFVIE in the homogeneous and layered media. It is discretized through the mixed-order basis function, i.e., the flux densities are expanded by the first-order roof-top functions, while the vector potentials are expanded by the second-order curl-conforming basis functions. The weak forms of CFVIE are solved by the BCGS-FFT iteration method. The results are compared to COMSOL simulations and it is verified that our forward scattering solver is accurate and reliable and has a significant efficiency advantage.

Then, we enhance the original VBIM by a self-adaptive regularization factor and use multifrequency data to obtain the multiscale resolution image in the inversion. The reconstructed Osterreich profile in the homogeneous background shows good resolution, although it degrades somehow in the through-wall model due to the smaller receiver array aperture. When the noise is added in the small but high-contrast scattering scenario, the basic locations and structures of scatterers can also be discerned, which show the good antinoise ability of our inversion method. One should notice that the influence of the antenna radiation pattern is not considered in this communication, and the current inversion algorithm is restricted by the nonlinearity of the problem caused by strong EM scattering, which will be left as future research.

APPENDIX

The expansion of (11) can be obtained by integrating each element in (12). We categorize the results from the integration. The detailed expressions are given in the following:

$$\begin{aligned} E_{3;m,n}^{inc} = & \frac{\epsilon_b}{\epsilon_{m,n}} d_{m,n}^{(3)} + j\omega\mu_b \sum_{i=1}^3 \sum_{j=1}^3 e_{i,j}^{(3)} a_{m,n,i,j}^{(3)} \\ & + \sum_{i=1}^3 \sum_{j=1}^2 u_{ij}^{(3)} f_{m,n,i,j}^{(2)} - \sum_{i=1}^2 \sum_{j=1}^3 v_{ij}^{(3)} f_{m,n,i,j}^{(1)} \end{aligned} \quad (19a)$$

$$\begin{aligned} H_{1;m,n}^{inc} = & \sum_{k=1}^3 c_k^{(1)} b_{m+k-2,n}^{(1)} \\ & + j\omega\epsilon_b \sum_{i=1}^2 \sum_{j=1}^3 (e_{ij}^{(1)} f_{m,n,i,j}^{(1)} + g_{ij}^{(1)} f_{m+1,n,i,j}^{(1)}) \end{aligned}$$

$$\begin{aligned} & + \frac{1}{j\omega\mu_b} \left[\sum_{i=1}^2 \sum_{j=1}^3 s_{ij}^{(1;1)} (f_{m,n,i,j}^{(1)} - f_{m+1,n,i,j}^{(1)}) \right. \\ & \left. + \sum_{i=1}^3 \sum_{j=1}^2 s_{i,j}^{(1;2)} (f_{m,n,i,j}^{(2)} - f_{m+1,n,i,j}^{(2)}) \right] \end{aligned} \quad (19b)$$

$$\begin{aligned} H_{2;m,n}^{inc} = & \sum_{k=1}^3 c_k^{(2)} b_{m,n+k-2}^{(2)} \\ & + j\omega\epsilon_b \sum_{i=1}^3 \sum_{j=1}^2 (e_{ij}^{(2)} f_{m,n,i,j}^{(2)} + g_{ij}^{(2)} f_{m,n+1,i,j}^{(2)}) \\ & + \frac{1}{j\omega\mu_b} \left[\sum_{i=1}^2 \sum_{j=1}^3 s_{ij}^{(2;1)} (f_{m,n,i,j}^{(1)} - f_{m,n+1,i,j}^{(1)}) \right. \\ & \left. + \sum_{i=1}^3 \sum_{j=1}^2 s_{i,j}^{(2;2)} (f_{m,n,i,j}^{(2)} - f_{m,n+1,i,j}^{(2)}) \right] \\ & + \sum_{i=1}^3 \sum_{j=1}^3 (u_{ij}^{(2)} a_{m,n,i,j}^{(3)} + v_{ij}^{(2)} a_{m,n+1,i,j}^{(3)}) \end{aligned} \quad (19c)$$

where

$$e^{(3)} = \frac{\Delta x_1 \Delta x_2}{36} \begin{pmatrix} 1 & 4 & 1 \\ 4 & 16 & 4 \\ 1 & 4 & 1 \end{pmatrix} \quad (20a)$$

$$u^{(3)} = \frac{\Delta x_2}{2} \begin{pmatrix} -1 & -1 \\ 0 & 0 \\ 1 & 1 \end{pmatrix} \quad (20b)$$

$$v^{(3)} = \frac{\Delta x_1}{2} \begin{pmatrix} -1 & 0 & 1 \\ -1 & 0 & 1 \end{pmatrix} \quad (20c)$$

$$c^{(1)} = \frac{\Delta x_1 \Delta x_2}{6} \begin{pmatrix} \frac{\mu_b}{\mu_{m,n}} & \frac{\mu_b}{\mu_{m+1,n}} \\ \frac{2\mu_b}{\mu_{m,n}} + \frac{2\mu_b}{\mu_{m+1,n}} & \frac{\mu_b}{\mu_{m+1,n}} \end{pmatrix} \quad (20d)$$

$$c^{(2)} = \frac{\Delta x_1 \Delta x_2}{6} \begin{pmatrix} \frac{\mu_b}{\mu_{m,n}} & \\ \frac{2\mu_b}{\mu_{m,n}} + \frac{2\mu_b}{\mu_{m,n+1}} & \\ \frac{\mu_b}{\mu_{m,n+1}} & \end{pmatrix} \quad (20e)$$

$$e^{(1)} = (e^{(2)})^T = \frac{\Delta x_1 \Delta x_2}{36} \begin{pmatrix} 1 & 4 & 1 \\ 2 & 8 & 2 \end{pmatrix} \quad (20f)$$

$$g^{(1)} = (g^{(2)})^T = \frac{\Delta x_1 \Delta x_2}{36} \begin{pmatrix} 2 & 8 & 2 \\ 1 & 4 & 1 \end{pmatrix} \quad (20g)$$

$$s^{(2;1)} = (s^{(1;2)})^T = \frac{1}{6} \begin{pmatrix} -1 & -4 & -1 \\ 1 & 4 & 1 \end{pmatrix} \quad (20h)$$

$$\frac{1}{\Delta x_1} u^{(1)} = \frac{1}{\Delta x_2} (u^{(2)})^T = \frac{1}{6} \begin{pmatrix} 0 & 0 & 0 \\ -2 & 0 & 2 \\ -1 & 0 & 1 \end{pmatrix} \quad (20i)$$

$$\frac{1}{\Delta x_1} v^{(1)} = \frac{1}{\Delta x_2} (v^{(2)})^T = \frac{1}{6} \begin{pmatrix} -1 & 0 & 1 \\ -2 & 0 & 2 \\ 0 & 0 & 0 \end{pmatrix}. \quad (20j)$$

REFERENCES

- [1] W. C. Gibson, *The Method of Moments in Electromagnetics*. Boca Raton, FL, USA: CRC Press, 2014.
- [2] L.-P. Song, E. Şimşek, and Q. H. Liu, "A fast 2D volume integral-equation solver for scattering from inhomogeneous objects in layered media," *Microw. Opt. Technol. Lett.*, vol. 47, no. 2, pp. 128–134, 2005.
- [3] Y. M. Wang and W. C. Chew, "An iterative solution of the two-dimensional electromagnetic inverse scattering problem," *Int. J. Imag. Syst. Technol.*, vol. 1, no. 1, pp. 100–108, Jun. 1989.
- [4] P. M. van den Berg and R. E. Kleinman, "A contrast source inversion method," *Inverse Problems*, vol. 13, no. 6, pp. 1607–1620, 1997.
- [5] X. Chen, "Subspace-based optimization method for solving inverse-scattering problems," *IEEE Trans. Geosci. Remote Sens.*, vol. 48, no. 1, pp. 42–49, Jan. 2010.
- [6] N. Zaiping, Y. Feng, Z. Yanwen, and Z. Yerong, "Variational Born iteration method and its applications to hybrid inversion," *IEEE Trans. Geosci. Remote Sens.*, vol. 38, no. 4, pp. 1709–1715, Jul. 2000.
- [7] G. Bellizzi, O. M. Bucci, and I. Catapano, "Microwave cancer imaging exploiting magnetic nanoparticles as contrast agent," *IEEE Trans. Biomed. Eng.*, vol. 58, no. 9, pp. 2528–2536, Sep. 2011.
- [8] Y. Chen, P. Kosmas, and S. Martel, "Microwave breast tumor detection and size estimation using contrast-agent-loaded magnetotactic bacteria," in *Proc. 35th Annu. Int. Conf. IEEE Eng. Med. Biol. Soc. (EMBC)*, Jul. 2013, pp. 5481–5484.
- [9] R. Persico and F. Soldovieri, "Two-dimensional linear inverse scattering for dielectric and magnetic anomalies," *Near Surface Geophys.*, vol. 9, no. 3, pp. 287–295, 2011.
- [10] G. Picardi *et al.*, "Radar soundings of the subsurface of Mars," *Science*, vol. 310, pp. 1925–1928, Dec. 2005.
- [11] Z. Yu, W. Zhang, and Q. H. Liu, "The mixed-order BCGS-FFT method for the scattering of three-dimensional inhomogeneous anisotropic magnetodielectric objects," *IEEE Trans. Antennas Propag.*, vol. 63, no. 12, pp. 5709–5717, Dec. 2015.
- [12] W. Zhang and Q. H. Liu, "Three-dimensional scattering and inverse scattering from objects with simultaneous permittivity and permeability contrasts," *IEEE Trans. Geosci. Remote Sens.*, vol. 53, no. 1, pp. 429–439, Jan. 2015.
- [13] W. C. Chew and J. H. Lin, "A frequency-hopping approach for microwave imaging of large inhomogeneous bodies," *IEEE Microw. Guided Wave Lett.*, vol. 5, no. 12, pp. 439–441, Dec. 1995.
- [14] W. Hu, A. Abubakar, and T. M. Habashy, "Simultaneous multifrequency inversion of full-waveform seismic data," *Geophysics*, vol. 74, no. 2, pp. R1–R14, 2009.
- [15] L.-P. Song, C. Yu, and Q. H. Liu, "Through-wall imaging (TWI) by radar: 2-D tomographic results and analyses," *IEEE Trans. Geosci. Remote Sens.*, vol. 43, no. 12, pp. 2793–2798, Dec. 2005.
- [16] W. Hu, A. Abubakar, and T. M. Habashy, "Joint electromagnetic and seismic inversion using structural constraints," *Geophysics*, vol. 74, no. 6, pp. R99–R109, 2009.
- [17] A. F. Peterson, S. L. Ray, and R. Mittra, *Computational Methods for Electromagnetics*. Hoboken, NJ, USA: Wiley, 1998.
- [18] K. A. Michalski and J. R. Mosig, "Multilayered media Green's functions in integral equation formulations," *IEEE Trans. Antennas Propag.*, vol. 45, no. 3, pp. 508–519, Mar. 1997.
- [19] H. A. van der Vorst, "Bi-CGSTAB: A fast and smoothly converging variant of Bi-CG for the solution of nonsymmetric linear systems," *SIAM J. Sci. Statistical Comput.*, vol. 13, no. 2, pp. 631–644, 1992.
- [20] P. Zwamborn and P. M. van den Berg, "A weak form of the conjugate gradient FFT method for two-dimensional TE scattering problems," *IEEE Trans. Microw. Theory Techn.*, vol. 39, no. 6, pp. 953–960, Jun. 1991.
- [21] F. Li, Q. H. Liu, and L.-P. Song, "Three-dimensional reconstruction of objects buried in layered media using Born and distorted Born iterative methods," *IEEE Geosci. Remote Sens. Lett.*, vol. 1, no. 2, pp. 107–111, Apr. 2004.